A Gait Simulation and Evaluation System for Hip Disarticulation Prostheses

Li Xinwei, Xiao Yixuan, He Chen, Hu Bingshan, and Yu Hongliu

***Abstract*— A little volume of lower extremity amputees needs hip disarticulation prostheses (HDPs). This situation makes it hard to invite hip amputees for prostheses test. The traditional evaluations for HDPs mostly refer to the questionnaires from the amputees and lack of quantitative criteria. In this article, we proposed a gait simulation and evaluation (GSE) system for HDPs testing. The GSE system contained a prosthetic thigh simulation robot that could reproduce the trajectory of human movement. We trained the simulation robot to walk with the tested HDPs using an adaptive neural network (ANN) control method. The ANN method was proposed to solve the unstable motion and large trajectory tracking error when the simulation robot was disturbed by the tested HDPs. The gait kinematic and kinetic data were collected to analyze the performance of the tested HDPs. The GSE system provided a stable test environment that opens up new possibilities for the HDPs test under controlled conditions.**

***Note to Practitioners*—Most of the prosthetic tests are based on amputees, especially hip disarticulation prostheses (HDPs). This work provides a gait simulation and evaluation system based on the quantified evaluation, which can repeatedly test the prostheses. The testing system improves the efficiency of the development of HDPs and decreases the security of the test with hip amputees. Furthermore, the system has backward compatibility for other lower limb prostheses (prosthetic knee and ankle).**

***Index Terms*— Adaptive neural network (ANN), gait simulation, hip disarticulation, prosthesis, quantitative criteria.**

I. Introduction

HIP disarticulation is an amputation removing the entire extremity through the hip joint capsule [1], [2]. Less than 1% of the amputees are either hip disarticulation or hemipelvectomy amputees. The amputations are often applied when malignancy, untreatable ischemia, or fulminant infection. The historical mortality rate of hip disarticulation exceeds 50% after the tumor resections [3], [4]. Besides the vascular and traumatic diseases, some injuries caused by low incidences, such as traffic accidents, electric stroke, and warfare injuries, also lead to hip disarticulation [5].

A number of studies were published to describe the developments of the hip disarticulation prostheses (HDPs) and its evaluation methods [6]–[8]. The general evaluating methods of HDPs were taking the subjective feeling of the amputees by questionnaire previously [9], [10]. The traditional methods of the HDPs evaluation have some limitations: low repeatability [11], [12], time-consuming [13], qualitative assessment [14], and difficulties in HD subjects recruitment [15], [16]. To investigate the energy consumption by the hip joint amputees with HDPs walking, Chin *et al.* [6] and Campbell and Robertson [17] recruited seven hip amputated subjects (more than 60 years old) to test the energy consumption of amputees with different HDPs. Their test progress was hard due to the terrible health condition of the subjects. In order to obtain more valuable results without the influence of the subjects' health condition, researchers from the Grenoble University Hospital tested the efficiency of the Helix^{3D} (a hydraulic HDP, from Otto Bock HealthCare GmbH, D). They collected the clinical data and walking parameters by inviting three young hip joint amputees [18], [19]. The test cost four days, which was a long-term experiment for the tested subjects. Schnall *et al.* [20] (from the Department of Veterans Affairs, USA) designed quantitative measures of energy cost and gait characteristics of a young soldier who was a unilateral traumatic hip amputated. However, only one subject's data analysis was not persuasive enough to evaluate the effectiveness and characteristics of prosthesis. Ludwigs *et al.* [5] analyzed the gait pattern of six hip joint amputees. The objective of his experiments was to compare two different prosthetic hip joints: Helix^{3D} and the 7E7. The kinematics and kinetics data were recorded by six charge-coupled cameras and two force plates [5], [21]. The externally produced sagittal moments were calculated with ground reaction forces (GRFs) and coordinates of joint axes.

Robotic testing introduced new concepts, designs, and control systems for prosthetic lower limbs' developments. Human subject test clearances, safety, and the lack of repeatability associated with human trials can be reduced or eliminated with automated testing. Many scientific research institutions have begun to develop special test platforms to test the prostheses instead of recruiting amputees for every test during the development of the prostheses [22]. In studies of prosthetic knees, many researchers utilized robotic equipment to simulate the thigh motion and evaluate their developing prosthetic knee performance. By the more efficient testing methods, they had achieved better results for the optimization of the

Manuscript received September 3, 2020; accepted October 5, 2020. This article was recommended for publication by Lead Guest Editor A. Si and Editor M. Zhang upon evaluation of the reviewers' comments. This work was supported in part by the Shanghai Engineering Research Center of Assistive Devices and in part by the National Key Research and Development Program, Manufacturing of key parts of lower limb prosthesis joints and molding process of carbon fiber energy storage foot plate, under Project 2018YFB1307303. *(Corresponding author: Yu Hongliu.)*

The authors are with the School of Medical Instrument and Food Engineering, University of Shanghai for Science and Technology, Shanghai 200093, China (e-mail: yhl98@hotmail.com).

Color versions of one or more figures in this article are available at https://doi.org/10.1109/TASE.2020.3035438.

Digital Object Identifier 10.1109/TASE.2020.3035438

prostheses [23], [24]. Cao *et al.* [25] tested a speed adaptive control method for a prosthetic knee during swing flexion with a robotic function simulation and evaluation platform. The platform had two main functions: 1) simulation of velocity changes and the real-time detection of knee angle and 2) imitation of the hip drive of the prosthetic knee to evaluate the swing performance [25]. Davis *et al.* [13] developed a tibia robot to test transfemoral prosthetic limbs [26]. The robot accurately simulated the motion of a human tibia and could test prostheses under different terrains. Unlike human tests, the robot provides a kind of testings in which prostheses could be tested under repeatable conditions. The robotic tests avoided liability and risk issues, which were common in the prostheses tests with amputees [13].

Beyond that, compared with the previous studies on the testing platforms for prosthetic knee and ankle [13], [23], the performances of prostheses were studied through standard quantitative parameters, and the problems of lower limb prosthesis could be proposed to advance down design improvements. Kim and Oh [23] and Davis [13] each developed their prosthetic test platforms for knee prosthesis research. The leg simulator designed by Kim and Oh [23] was used to test the joint position and velocity of an above-knee prosthesis. The simulator had only three DOFs, including the hip flexion/extension and the knee joint angle, which ignored that the human body gravity center changes had effects on lower extremity movements. However, normal walking not only consists of the movement of the extension and flexion of the thigh but also includes the movement of the hip joint with the connection to the pelvis in the space. The movement of the thigh can be taken as a composition of these two movements. Therefore, in the process of ground interactive prosthesis testing, it was not comprehensive to only consider the hip joint as a fixed swing joint but neglect the change of human body gravity center. The trunk applies the force to legs during walking affected the kinetic performances of the tested prostheses. Our research suggested that the human body gravity center's movement should not be neglected during the lower limb prostheses test. A tibia robot was used to optimize the GRF of transfemoral prosthetic limbs by the research team of Davis *et al.* [13]. Their research solved such an unknown nonlinear dynamic system and took the interface force/torque as optimization references of robotic HDP.

The objectives of this research are to solve the problems in the current HDPs research and tests, including: 1) lack of amputees for the prosthetic tests; 2) the safety of the hip disarticulation subjects could not be guaranteed at the preliminary research stage; and 3) quantitative and repeatable parameters could not be obtained systematically with the hip disarticulation subjects. Therefore, we developed a prosthetic gait simulation and evaluation (GSE) system that could simulate the pelvic track in natural human gait and drag the HDPs to walk on a treadmill. An adaptive neural network (ANN) control method was proposed to solve the problem of unstable motion and large trajectory tracking error when the manipulator was disturbed by the dragged HDPs.

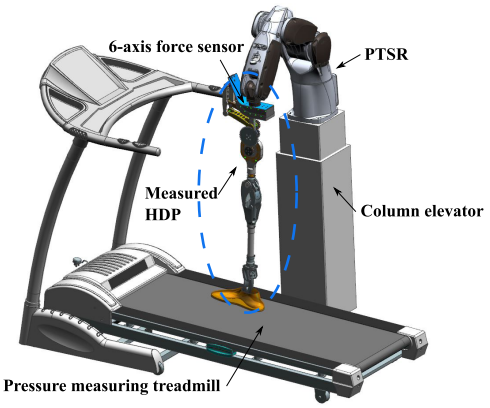

Fig. 1. Compositions of the GSE system. The tested prostheses (HDP, prosthetic knee, and foot) are in the blue dotted oval.

TABLE I
D-H PARAMETERS OF PTSR

Link	θ	d (m)	a (m)	α (rad)	m (kg)
1	θ_1	0.365	0.07	$-\pi/2$	6.78
2	θ_2	0	0.285	0	8.33
3	θ_3	0	0.04	$-\pi/2$	3.97
4	θ_4	0.279	0	$\pi/2$	3.41
5	θ_5	0	0	$-\pi/2$	1.79
6	θ_6	0.106	0	0	0

II. METHODS

A. Gait Simulation and Evaluation System

The GSE system, as shown in Fig. 1, contains a prosthetic thigh simulation robot (PTSR), a six-axis force sensor, and a pressure measuring treadmill. The treadmill was used to analyze the GRF. The PTSR for pelvic trajectory reproduction was six degrees of freedom (DOFs) manipulator (RT-Sim simulator, Beijing Links Co., Ltd.) and its D-H parameters were listed in Table I. In the structure of the system, as shown in Fig. 2, the trajectory data collected by the camera-based motion analyzer are smoothed by a Gaussian smoother. The smoothed trajectory is mapped into the PTSR workspace with an alignment of PTSR's initial position. The tested HDP and the end-effector of PTSR were connected rigidly with a six-axis force sensor (M3713B, Sunrise Instruments Co., Ltd.). The force sensor could monitor the interface force/torque between the tested HDP and the PTSR. The direction of six forces/torques was presented in Fig. 3. A pressure measuring treadmill (FDM system, zebris Medical Gmbh, German) was used to set constant speed and measured the GRF of the prostheses. Finally, the final joints' information of PTSR is reordered by the ANN controller to improve the stability of the end-effector. As the lengths of the whole measured prosthetic legs (including the thigh, shank, and foot), were not the same, a column elevator was used to adjust the PTSR's basement height.

The gait parameters studied in this research could be divided into three categories: kinematics, kinetics, and mutual information [12]. The kinematic parameters included joint

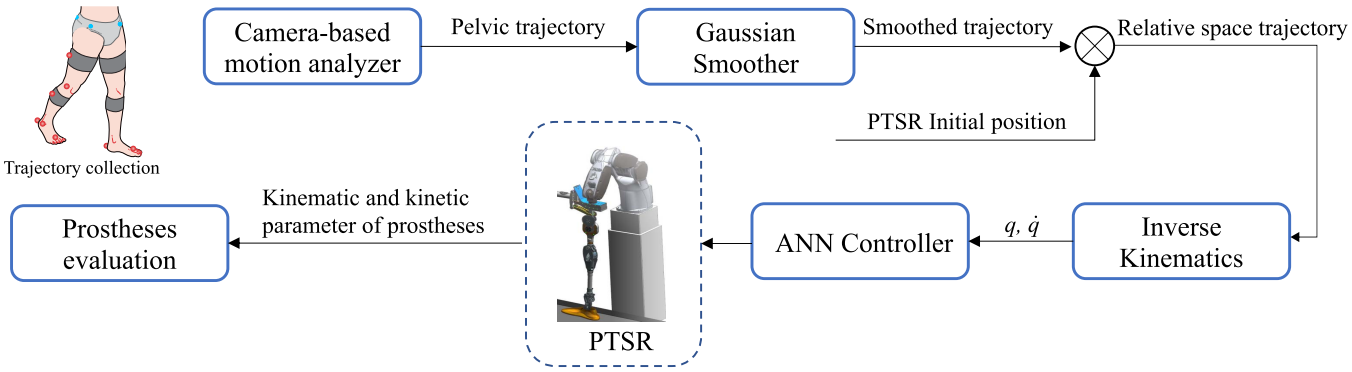

Fig. 2. Structure of the GSE system. The trajectory data collected by the camera-based motion analyzer are smoothed by a Gaussian smoother. The smoothed trajectory is mapped into the PTSR workspace with an alignment of PTSR initial position. Finally, the final joints' information of PTSR is reordered by the ANN controller to improve the stability of the end-effector.

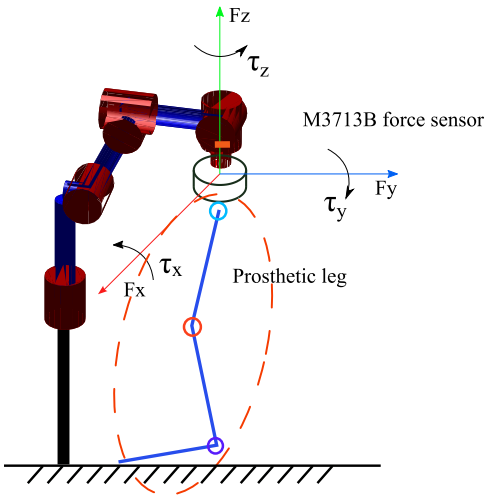

Fig. 3. Introduction of multidimensional force collection with M3713B.

angle, angular velocity, and walking speed. The kinetic parameters contained angular acceleration and joint torque. The monitored mutual information included plantar pressure and 6-D interface force/torque at the end-effector of PTSR. Furthermore, symmetry analysis could be conducted with the contrast between the original gait data and the collected parameters.

B. ANN Tracking Control for PTSR

The ANN was widely used in nonlinear system control, such as machining and grinding on the industrial production line, and trajectory planning in autopilot, in order to obtain better stability [27]. Except for the original data smoothing, an ANN tracking control was proposed to solve prosthetic kinetics uncertainties and improve PTSR's robustness.

Considering the dynamic equation of the six-DOF PTSR to a lumped disturbance and delayed states described by the following nonlinear differential equation:

$$M_j(q)\ddot{q} + C_j(q,\dot{q})\dot{q} + G_j(q) = \tau - \tau_{ds} \tag{1}$$

where $M_j(q)$ is the symmetric positive definite inertial matrix, $C_j(q,\dot{q})\dot{q}$ is the vector of coupled Coriolis and centripetal torques, $G_j(q)$ is the vector of gravitational torques, τ is the vector of joint torques, τ_{ds} is the vector of external disturbance torques, and q, $\dot{q}$, and $\ddot{q}$ are the vectors of the joint displacement, velocity, and acceleration, respectively. The forward kinematics can be written as

$$\xi = \Phi(q), \quad \dot{\xi} = J(q)\dot{q}. \tag{2}$$

Thus, the backward kinematics can be written as

$$\begin{aligned} \dot{q} &= J_I(q)\dot{\xi} \\ \ddot{q} &= \dot{J}^{-}(q)\dot{\xi} + J_I(q)\ddot{\xi} \end{aligned} \tag{3}$$

where $J(q)$ is the Jacobian matrix of PTSR, $J_I(q) \in \mathbf{R}^{n\times m}$ is the generalized inverse matrix of $J(q)$, and $\xi, \dot{\xi}, \ddot{\xi} \in \mathbf{R}^m$ represent the displacement, velocity, and acceleration in the task space. According to the abovementioned transformations, the dynamics (1) is converted as

$$M_t(\xi)\ddot{\xi} + C_t(\xi,\dot{\xi})\dot{\xi} + G_t(\xi) = u - f \tag{4}$$

where $M_t(\xi)$ is the symmetric positive definite inertial matrix, $C_t(\xi,\dot{\xi})\dot{\xi}$ is the vector of the coupled Coriolis and centripetal torques, $G_t(\xi)$ is the vector of the gravitational torques, u is the force of the manipulator end-effector, and f is the disturbance from the tested HDPs. From the joint space to the task space, the related matrices are formulated as

$$\begin{aligned} M_t(\xi) &= J_I^T(q)M_j(q)J_I(q) \\ C_t(\xi,\dot{\xi}) &= J_I^T(q)[C_j(q,\dot{q})J_I(q) + M_j(q)\dot{J}(q)] \\ G_t(\xi) &= J_I^T(q)G_j(q) \\ u &= J_I^T(q)\tau. \end{aligned} \tag{5}$$

Considering that the robot dynamics model is known and $x_1 = q$ and $x_2 = \dot{q}$ are defined, (2) is converted to state space form

$$\begin{aligned} \dot{x}_1 &= x_2 \\ \dot{x}_2 &= M_j^{-1}(x_1)(\tau - \tau_d - C_j(x_1,x_2)x_2 - G_j(x_1)). \end{aligned} \tag{6}$$

Define the Cartesian space signals as

$$e_1 = x_1 - x_d \tag{7}$$

$$\alpha_1 = -K_1 e_1 + \dot{x}_d \tag{8}$$

$$e_2 = x_2 - \alpha_1. \tag{9}$$

$\dot{e}_1$ and $\dot{e}_2$ are derived by (7) and (9) as

$$\begin{aligned}\dot{e}_1 &= e_2 + \alpha_1 - \dot{x}_d \\ \dot{e}_2 &= M_j^{-1}(x_1)(\tau - \tau_d - C_j(x_1, x_2)x_2 - G_j(x_1)) - \dot{\alpha}_1. \quad (10)\end{aligned}$$

During the HDP testing, the inertia matrix $M_j(q)$ and the vector of coupled Coriolis and centripetal torques $C_j(q, \dot{q})\dot{q}$ are uncertain [16]; here, we use $M_{jd}(q)$ and $C_{jd}(q, \dot{q})\dot{q}$ to represent the defined reference matrix. The uncertain inertia and Coriolis parts $M_{ju}(q)$ and $C_{ju}(q, \dot{q})\dot{q}$ are as follows:

$$\begin{aligned}M_j(q) &= M_{jd}(q) + M_{ju}(q) \\ C_j(q, \dot{q}) &= C_{jd}(q, \dot{q}) + C_{ju}(q, \dot{q}). \quad (11)\end{aligned}$$

Taking the interaction torque between the PTSR and the tested HDPs τ_{HDP} into consideration, the Cartesian space dynamic neural network based on adaptive control is modified, supposing the dynamic model, by adding the τ_{HDP}, to

$$\tau_f = -e_1 - K_2 e_2 + \hat{\tau}_d + \hat{\kappa}^{\mathrm{T}}\psi(Z) + C_{jd}(x_1, x_2)\alpha_1 + \tau_{\mathrm{HDP}} \quad (12)$$

where $\psi(Z)$ represents the radial basis function (RBF) neural network, κ^{T} is the weight estimation, and $Z = [x_1^{\mathrm{T}}, x_2^{\mathrm{T}}, \dot{e}_2^{\mathrm{T}}, \dot{\alpha}_1^{\mathrm{T}}]$. The optimal weight κ^* is constructed for easy deduction

$$\kappa_i^* = \arg\min_{\kappa_i \in R^i} \left\{ \sup_{Z \in \Omega_X} |\nu_i(Z)| \right\} \quad (13)$$

where $\nu_i(Z) \in \mathrm{R}^n$ is the estimation error and $\tilde{\kappa} = \kappa^* - \hat{\kappa}$ is the weight error. Here, we estimate $\hat{\kappa}^{*\mathrm{T}}\psi(Z)$ by $\hat{\kappa}^{\mathrm{T}}\psi(Z)$

$$\begin{aligned}\kappa^{*\mathrm{T}}\psi(Z) = M_j(x_1)\dot{\alpha}_1 + C_{ju}(x_1, x_2)x_2 \\ + G_j(x_1) + M_{ju}(x_1)\dot{e}_2 - \nu(Z) \quad (14)\end{aligned}$$

and the adaptive law of neural network $\dot{\hat{\kappa}}_i$

$$\dot{\hat{\kappa}}_i = -\Gamma_i(\psi_i(Z)e_{2,i} + \sigma_i\hat{\kappa}_i) \quad (15)$$

where σ_i is a small positive constant and Γ_i is a symmetric positive matrix; considering (10) and (14), we have

$$\begin{aligned}\dot{e}_2 = M_{jd}^{-1}(x_1)(\tau_f - \tau_d - C_{jk}(x_1, x_2)x_2 \\ - \kappa^{*\mathrm{T}}\psi(Z) - \nu(Z)). \quad (16)\end{aligned}$$

Another assistive variable e_3 is defined as

$$e_3 = \chi(e_2) + \tau_d. \quad (17)$$

Take the derivative of e_3 to get

$$\begin{aligned}\dot{e}_3 &= \dot{\tau}_d + R(e_2)\dot{e}_2 \\ &= \dot{\tau}_d + R(e_2)M_{jd}^{-1}(x_1) \\ &\quad \times (\tau_f - \tau_d - C_{jk}(x_1, x_2)x_2 - \kappa^{*\mathrm{T}}\psi(Z) - \nu(Z)) \quad (18)\end{aligned}$$

where $R(e_2)$ is the derivate of $\chi(e_2)$ with respect to e_2

$$\dot{\hat{e}}_3 = R(e_2)M_{jd}^{-1}(x_1)(\tau_f - C_{jk}(x_1, x_2)x_2 - \hat{\tau}_d) \quad (19)$$

where $\hat{e}_3$ is the estimation of e_3 and could be get from

$$\hat{\tau}_d = \hat{e}_3 - \chi(e_2). \quad (20)$$

From (24) and (27), we have

$$\tilde{\tau}_d = \tau_d - \hat{\tau}_d = e_3 - \hat{e}_3 = \tilde{e}_3. \quad (21)$$

From the abovementioned analysis

$$\dot{\tilde{\tau}}_d = \dot{\tau}_d - R(e_2)M_{jd}^{-1}(x_1)(\tilde{\tau}_d + \kappa^{*\mathrm{T}}\psi(Z) + \nu(Z)). \quad (22)$$

The error signals, e_1, e_2, $\tilde{\tau}_d$, and $\tilde{\kappa}$, are proved to be semiglobal uniform bounded as Proof 1 in the Appendix.

III. Experiments

The subject test was approved by the Ethics Committee of the Shanghai University of Medicine and Health Science (No. 2019-ZYXM1-04-420300197109053525); the experimental nature and possible risks were informed of the subjects; and the final consent was obtained from the subjects.

A. Gait Test With Amputee

The purpose of testing hip disarticulated subject's gait was to adjust whether the gait and pelvic trajectory data were suitable for the GSE system to evaluate the performance of different HDPs (refer to Table II). Here, we use symmetry index (SI) of the gait to estimate the gait of hip disarticulation subject [28]

$$SI = \frac{2(X_R - X_L)}{X_R + X_L} \times 100\% \quad (23)$$

where X_R is the right limb data and X_L is the corresponding data for the left limb. The prosthetic leg side was X_L, and the healthy side was X_R in this work. X_R and X_L represented different kinds of the lower limb data (including the joint angle, velocity, torque, and GRF) for different SI calculations but not an isolated parameter that is measured by a sensor. SI = 0 represents the perfect symmetry and ± showing limb dominance.

In each gait cycle, the average hip angle SI was less than 0.2, and the average knee angle SI does not exceed 0.15, which was an acceptable gait symmetry range for the GSE system. First, we collected the gait parameters of a hip disarticulated subject by a real-time motion analysis system (Jiangsu NEUCOGNIC MEDICAL Co., Ltd.) and the FDM system. The experimental sense of amputee testing on the treadmill can be seen in Fig. 4. During the walking experiments, the prosthetic leg for the amputated subject consisted of a prosthetic foot (1C10 Terion, Otto Bock HealthCare GmbH, D), a prosthetic knee (3R60, Otto Bock HealthCare GmbH, D), and a traditional hip prosthesis (7E7, Otto Bock HealthCare GmbH, D). From the analysis of the gait data, the mean SI values of the amputated subject's bilateral hip joints in the stance and swing phase were 35.8% and 23.7%, respectively, which exceeded the acceptable symmetry range. The gait of the amputee wearing the original uniaxial hip amputation prosthesis was asymmetric pathologic according to the gait symmetry measurements. Therefore, it was ineffective to test the HDPs with the gait data of the amputees.

We studied the possibility of taking the gait data of a nonamputee instead of the amputees. The recruitment standard was that the body shape of the nonamputees should be similar to the amputated subject (including the height and weight). This system's ultimate goal is to train the newly developed and intelligent prosthesis based on a standard trajectory test

TABLE II
PARAMETERS OF THE TEST HDPs

Name	Weight(g)	Motion range(°)	Drive form	Joint mechanism category	Max. support(kg)
Otto 7E7	875	130	passive-spring	single axis	100
Helix^{3D}	990	130	passive-hydraulic	polycentric	100
RCM HDP	2460	145	active-motor	single axis	120

Fig. 4. Hip disarticulated amputee test on the treadmill.

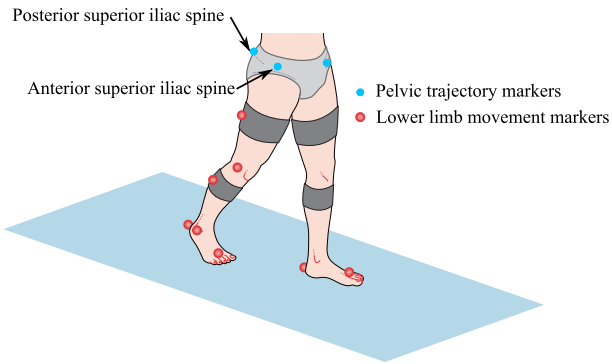

Fig. 5. Markers' position in a normal walking gait cycle test.

TABLE III
TESTED SUBJECTS' CHARACTERISTICS

	Gender	Age(years)	Height(cm)	Weight(kg)	mean $SI(\%)$
HD	M	31	175	60	29.75
H1	M	26	177	72.5	15.31
H2	M	27	176	79	17.64

HD represents the hip disarticulated subject
H1 and H2 represent the two healthy subjects

reproducing so that it can help the amputee recover a more symmetrical gait. Moreover, if those trajectories are used to train the prosthesis and optimize the intelligent prostheses' parameters, the optimized prosthesis cannot approach the athletic performance of the sound side. The previous experiment by the HD subject is to illustrate that it is inadvisable to test the prostheses with the trajectory of the amputated side.

The healthy data would be more suitable for exploring the control strategy of the prosthesis. The basic gait parameters of healthy subjects under constant speed were obtained through experiments. In the nonamputee gait data collection experiments, two subjects were recruited, and the detailed information of them was shown in Table III.

The pelvic trajectories of nonamputees were collected by the camera-based motion analyzer (Vicon, Oxford, U.K.). After the calibration of the test system, the markers were attached to the measurement points (skin) of the subjects, respectively, on the toe, heel, ankle, calf, knee, thigh, anterior superior iliac spine, and posterior superior iliac spine (see Fig. 5).

The subjects were required to walk on the test platform several times, and their gait data were collected after they adapted to the platform. During the experiments, the nonamputees were instructed to walk on the treadmill at speeds of 0.5, 1, and 1.2 m/s, respectively. The data collected from the motion analyzer often contain unwanted noise. This noise was generated by the process being monitored and the measurement system itself. To eliminate the noise of joint velocity and acceleration, the Gaussian scale space was employed to smooth the raw data.

The human pelvic trajectories reproducing method proposed in this study is based on position-time information. Given the influence of human body weight on the parameter assessment, the authors agree that, under some same experimental conditions, such as walking speed, human body weight would inevitably cause the change of motion parameters of prostheses. However, this study aimed to compare different HDPs under the same experimental conditions (including the human body weight) as possible. Therefore, as long as the bodyweight of the tested subjects is in the maximum support range of HDPs, this research's experimental requirements will be met.

B. HDPs Tests by the GSE System

In the experiments, the kinematic, kinetic, and mutual parameters of the tested HDPs were collected. Three different HDPs: 1) Otto Bock HealthCare GmbH, D; 2) Helix^{3D} (Otto Bock HealthCare GmbH, D); and 3) RCM HDP (from the authors' research team) were tested by the GSE system at the at speeds of 0.5, 1, and 1.2 m/s, respectively. The parameters of the three HDPs were listed in Table II. Considering the significance of the experiment to the later adaptation of the HDPs, 1C10 Terion (Otto Bock HealthCare GmbH, D) was selected as the foot, and 3R60 (Otto Bock HealthCare GmbH, D) was selected as the knee for the measurements. During the test of three HDPs, the prosthetic knee joint and ankle joint are fixed. In order to ensure that the overall sizes of the

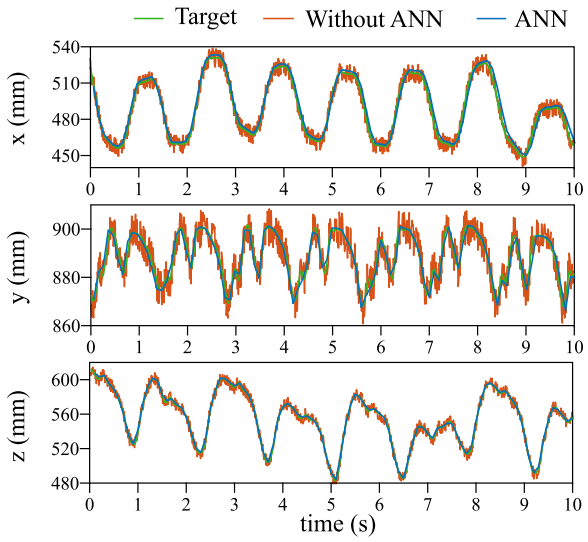

Fig. 6. Statistical results on pelvis position tracking of PTSR in three planes (x, y, and z refer to sagittal, coronal, and frontal planes).

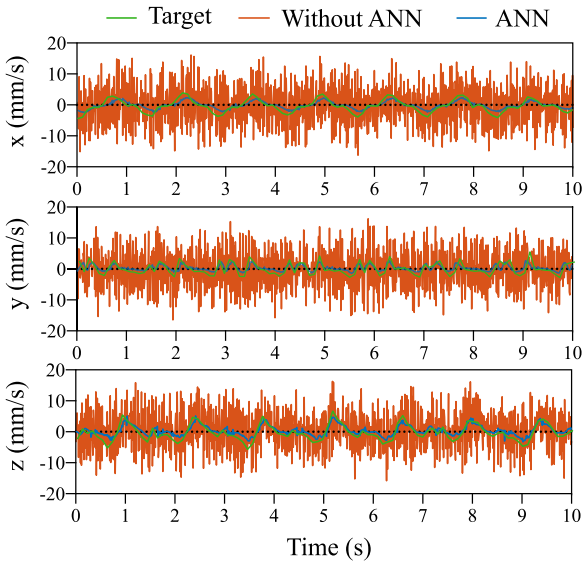

Fig. 7. Statistical results on pelvis velocity tracking of PTSR in three planes (x, y, and z refer to sagittal, coronal, and frontal planes).

three prosthetic systems are consistent with each other, three thigh tubes that were used to connect the HDPs and prosthetic knee were customized with different sizes. The parameters including pelvic trajectory, kinematic parameters of the HDPs (joint angle and velocity), kinetic parameters of hip torque, interface force/torque between PTSR and the HDPs, and GRF with pressure testing treadmill were collected for analysis.

IV. Results and Discussion

A. Results

1) Pelvic Trajectory: Fig. 6 indicated the position tracking of the pelvic trajectories in direct position mode and ANN compensating mode in space under the walking speed of 1 m/s. Compared with the direct position control, the tracking error of the pelvic trajectories under ANN compensating mode was decreased by 45.2%, 37.1%, and 39.3% ($p < 0.05$) in sagittal, coronal, and frontal planes, respectively. The average position tracking error under the speed of 0.5 and 1.2 m/s was also decreased by 34.9% and 41.6%, respectively.

Fig. 7 indicated the velocity tracking of the pelvic trajectories in direct position mode and ANN compensating mode in space under the walking speed of 1 m/s. Compared with the direct position control, the tracking error of the pelvic velocity under ANN compensating mode was decreased by 38.9%, 27.6%, and 40.5% ($p < 0.05$) in sagittal, coronal, and frontal planes, respectively. The average velocity tracking errors under the speed of 0.5 and 1.2 m/s were also decreased by 29.3% and 38.2%, respectively.

2) Gait Symmetry: Fig. 10 shows the mean symmetry index of gait parameters. The symmetry index of the measured prosthesis is the degree of symmetry between kinematic and dynamic parameters of the prosthesis and the original trajectory acquisition experiment by the able-bodied subjects. The symmetries of the prostheses' kinematic parameters were improved in different scales. The mean symmetries of the joint angle and angular velocity are increased by 10.5% and 11.7% ($p = 0.009$), respectively. The mean symmetries of the joint torque and GRF were significantly increased by 8% and 6% ($p = 0.013$), respectively. It was found that the ANN method for pelvic trajectory simulation effectively improved the symmetry of kinematic and kinetic performances of the tested HDPs compared with the direct position control.

3) Kinematic and Kinetic Parameters of the HDPs: Fig. 8 shows the angles and joint velocities of three tested HDPs. Due to little damping of the passive HDPs, the joint accelerations of those HDPs were larger than RCM HDP at the beginning of the stance phase by 20%–33%. The joint angle and velocity of RCM HDP were more similar to the gait of the nonamputees. The mean joint angle of RCM HDP was significantly bigger than 7E7 and Helix^{3D} by 21.5° and 17.3° ($p = 0.013$), respectively. The maximum extension of RCM HDP reached 55% of a whole gait cycle. This was approximately close to the nonamputees (at 60%) rather than other HDPs (at 21%). Until the flexion was initiated after 70% of the gait cycle, the hip angle of 7E7 and Helix^{3D} changed to the extension. However, the flexion started at the end of the maximum extension straight away with the RCM HDP at 55% of the gait cycle on average. For power saving, the maximum extension of RCM HDP was limited to 110°, which satisfied the amputees' walking requirements. The moments from −0.15 (flexion) to 0.46 Nm/kg (extension) produced by RCM HDP during stance mostly were active moments (as shown at the bottom of Fig. 8). This kind of active moment represented the robustness of the prosthesis. Due to limitations of the prosthetic system dynamics model, the passive moments of 7E7 and Helix^{3D} were not achieved by the GSE system.

4) Interface Force/Torque Between PTSR and HDPs: The mean (and standard deviation) values of the interface force/torque collected by M3713B under different walking speeds were listed in Table IV. From the test results, both interface force and torque increased with the increase in the walking speed, especially the mean force of the z-axis, F_z,

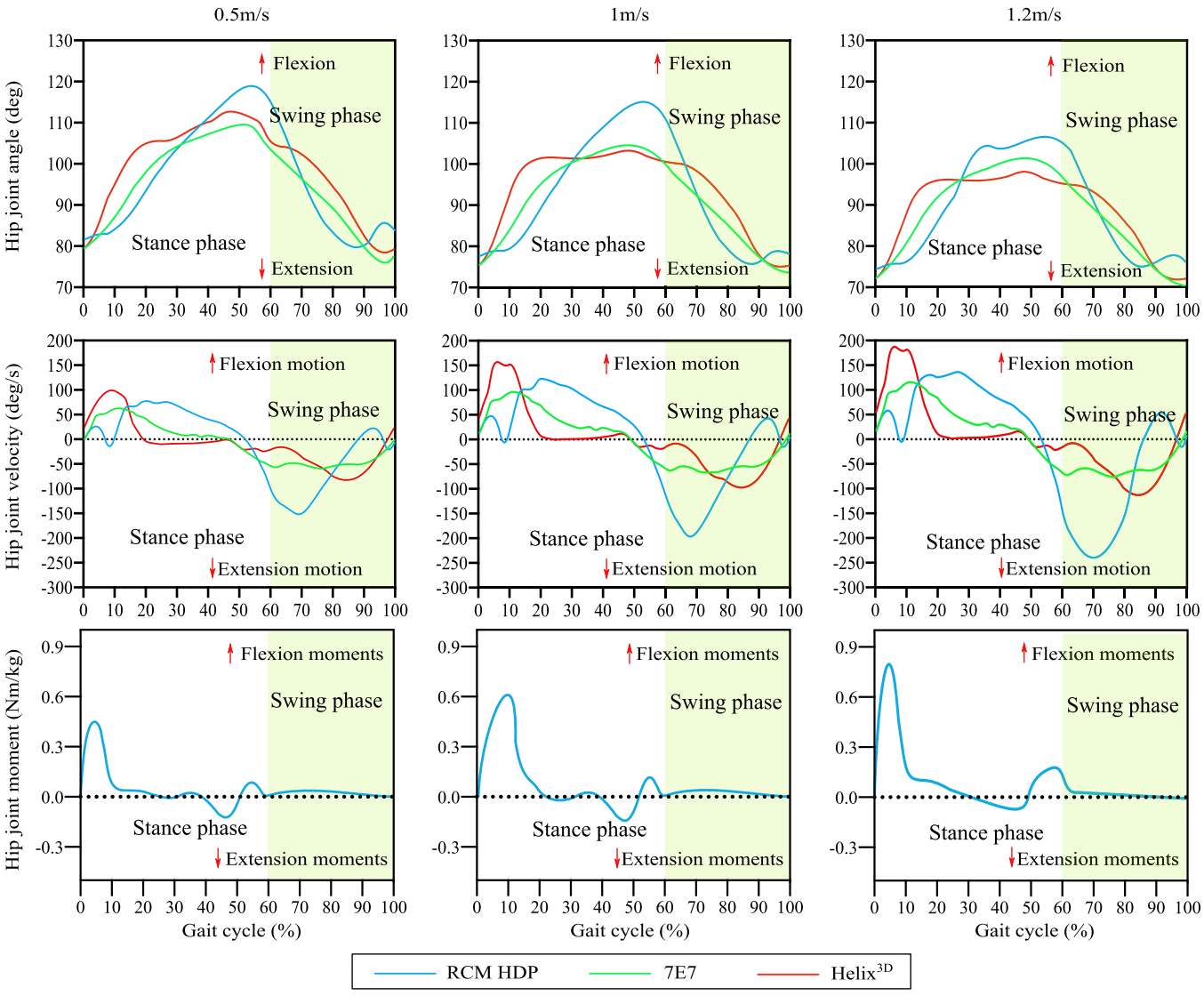

Fig. 8. Mean kinematic and kinetic parameters of the tested HDPs (angle, velocity, and moment). *significant, and $p < 0.05$.

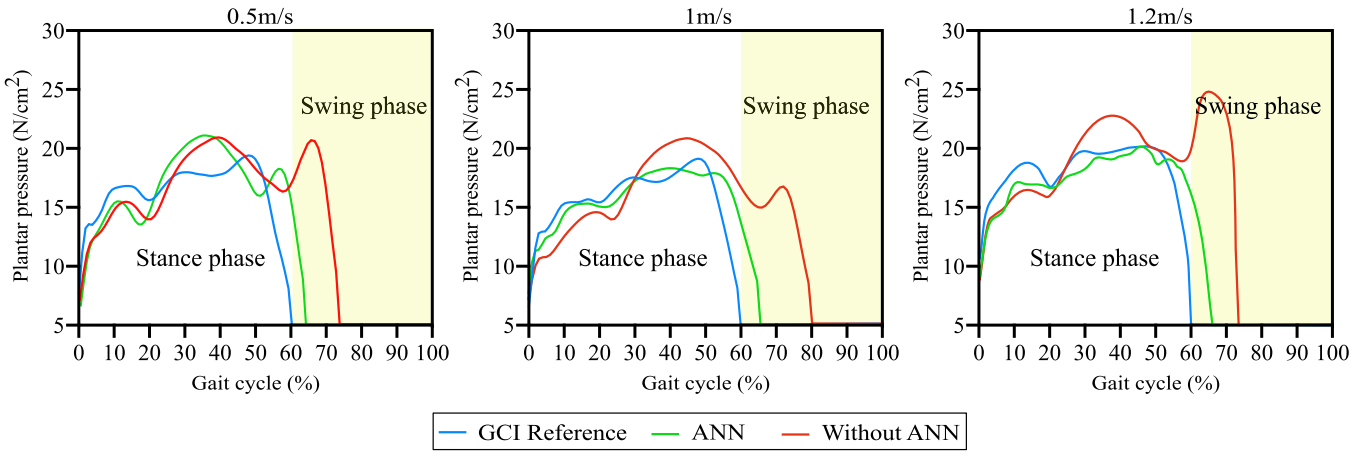

Fig. 9. Mean GRF of three tested HDPs. *significant, and $p < 0.05$.

and the mean torque around the y-axis, τ_y. The mean force of the z-axis, F_z, in a gait cycle ranged from 50 to 62 N, which was the maximum force direction of the interface. The mean torque around the y-axis has changed in the biggest range from

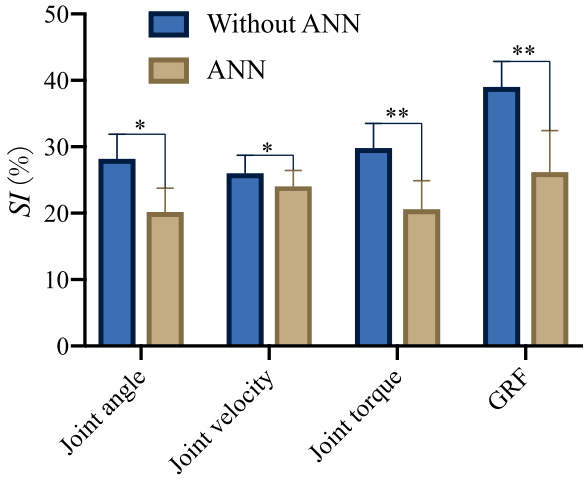

Fig. 10. Symmetry of the ground GRF during the prosthetic test. *significant, $p < 0.01$, **significant, and $p < 0.015$.

TABLE IV
MEAN INTERFACE FORCE/TORQUE (AND STANDARD DEVIATION) BETWEEN PTSR AND 7E7

		speed(m/s)		
		0.5	1	1.2
Mean Force (N)	fx	10.51(0.81)	11.42(0.91)	12.39(0.12)
	fy	11.39(2.63)	13.91(3.09)	17.30(2.27)
	fz	50.26(4.54)	55.63(3.95)	61.47(5.15)
Mean Torque (Nm)	τ_x	0.38(0.048)	0.26(0.08)	0.42(0.014)
	τ_y	1.54(0.19)	3.13(0.07)	4.67(0.15)
	τ_z	1.09(0.67)	1.45(0.31)	1.22(0.03)

1.54 to 4.67 Nm because the main motion of the tested HDPs was in the sagittal plane.

5) Ground Reaction Force: Fig. 9 shows the mean GRF of Otto 7E7 collected by zebris pressure measuring treadmill, at speeds of 0.5, 1, and 1.2 m/s, respectively. The maximum GRF in common practice could be found in the middle of the stance phase. Under the ANN control, the mean GRF between 7E7 and treadmill was significantly larger than the value under the direct position control by 5 N/cm^2 ($p = 0.023$) at the end of the stance phase. Especially at higher speed, the maximum plantar force of the tested HDP was increased by 7 N/cm^2, which meant the stable tracking contributed to the ideal environment contacts of the tested HDPs. Each gait cycle of the unilateral leg could be divided into the swing phase and stance phase according to whether the foot is in contact with the ground or not. For ordinary subjects, the swing phase accounted for around 60% of the gait cycle, and the stance phase accounted for 40%, respectively. From the GRF analysis, the ANN method for PTSR increased the swing phase initiation by 11.34% ($p = 0.018$) on average compared with the direct position control. The proportion between the two gait phases with ANN was closer to standard data from GCI references than direct position control by 24.86% ($p = 0.027$) on average.

B. Discussion

This study developed a GSE system that could simulate the pelvic track in human natural gait and drag the HDPs as pelvic does to test the HDPs. The experimental results proved the feasibility of testing prostheses with the robotic system instead of amputees only.

The pelvic trajectory reproducing was proven to be stable in the position and speed loop, as shown in Figs. 6 and 7. In comparison with the previous tests, the proposed GSE system precisely solved the problems: low repeatability [11], [12], time-consuming [13], qualitative assessment [14], and difficulties in HD subjects recruitment [15], [16]. The stable repetition of the pelvic trajectory indicated that our approach for testing prosthetic components was effective and valid. The kinematic and kinetic parameters of the tested HDPs during the tests could be easily collected, as shown in Figs. 8 and 9. These safety and dynamic parameters of the prostheses could be utilized to verify and optimize the tested HDPs before the tests participated with amputated subjects.

From the results of GRF (see Fig. 9) and symmetry index (see Fig. 10), this study found that the ANN control was effective in handling the unknown nonlinear dynamic system. When the end-effector of the PTSR was in a rigid connection with the tested HDPs, the ANN control had a better performance than direct position control and significantly improved the GRF and symmetry of the tested HDPs. From the GRF analysis, the ANN method for PTSR increased the swing phase initiation compared with the direct position control. The ANN method made the proportion between two gait phases closer to standard data of GCI references than direct position control. The GRF of prosthetic legs characterized the walking stability of the amputees. It was required to be symmetric to the intact side as well. The low plantar pressure indicated that the stability of the stance phase was insufficient, and it was prone to fall and other safety problems. Excessive plantar pressure showed that the vibration absorption capacity of each joint was insufficient during the contact between the prosthetic side and the ground. Without considering the prosthetic knee and ankle, for the nondynamic hip prosthesis, the hip joint damping could be adjusted to reduce the GRF, whereas, for the dynamic hip prosthesis, the impedance control was needed to improve the flexibility of the active hip joint by replacing the position-velocity control. The SI of the optimized active HDP GRF was still up to 31.5%, which was difficult to meet the target value.

There were still some limitations of this research to be solved. First, the stance phase of the tested prostheses was longer than the reference data from the GCI data set in the GRF results' aspect. The main reason for the asymmetry was that the trajectory reproducing based on the position-time strategy and the track acceleration in the sagittal plane is different from the normal human body's actual acceleration. Normal walking consists of the movement of the extension and flexion of the thigh and includes the movement of the hip joint with the connection to the pelvis in the space. The movement of the thigh can be taken as a composition of these two movements. Therefore, in the process of ground interactive

prosthesis testing, it is not comprehensive to only consider the hip joint as a fixed swing joint but neglect the change of human body gravity center. The inertial movement in the center of gravity of the human body's sagittal plane should be considered to counteract the different accelerations caused by the previous trajectory reproducing method. Second, the pelvic trajectories collected from the camera-based motion analyzer should be smoother for reproduction.

V. Conclusion

This article developed a GSE system that can simulate the pelvis motion to test different HDPs with a PTSR. The proposed ANN solved the unstable motion and large trajectory tracking error when the simulation robot was disturbed by the tested HDPs. The performance of the simulation robot was consistent with the proof of the closed-loop system stability and convergence. The GSE system provided a safe test environment that cannot be obtained with human subjects.

The robotic testing opened up new possibilities for prosthetic tests under controlled conditions. In particular to the hip disarticulated amputees, the personal customized HDP for them was an open research question in further work. This simulation method of the human body feature point movement can be utilized to repeatedly evaluate multiple wearable types of equipment under the same testing environment without real subjects.

Appendix

Proof 1: Consider the Lyapunov function candidate

$$V_1 = \frac{1}{2}e_1^{\mathrm{T}}e_1 + \frac{1}{2}e_2^{\mathrm{T}}M_{jd}(x_1)e_2 + \frac{1}{2}\sum_{i=1}^{n}\tilde{\kappa}_i^{\mathrm{T}}\Gamma_i^{-1}\tilde{\kappa}_i + \frac{1}{2}\tilde{\tau}_d^{\mathrm{T}}\tilde{\tau}_d. \quad (24)$$

The time derivative of V_1 is

$$\begin{aligned}\dot{V}_1 \le\ & -e_1^{\mathrm{T}}K_1e_1 + \tilde{\tau}_d^{\mathrm{T}}\dot{\tau}_d - \tilde{\tau}_d^{\mathrm{T}}R(e_2)M_{jd}^{-1}(x_1)\nu(Z) \\ & - \tilde{\tau}_d^{\mathrm{T}}R(e_2)M_{jd}^{-1}(x_1)\tilde{\tau}_d - \tilde{\tau}_d^{\mathrm{T}}R(e_2)M_{jd}^{-1}\sigma^{*\mathrm{T}}\psi(Z) \\ & + e_2^{\mathrm{T}}(-K_2e_2 + \tilde{\tau}_d + \hat{\kappa}^{\mathrm{T}}\psi(Z) - \kappa^{*\mathrm{T}}\psi(Z) - \nu(Z)) \\ & + \sum_{i=1}^{n}\tilde{\kappa}_i^{\mathrm{T}}\Gamma_i^{-1}\dot{\hat{\omega}}_i. \end{aligned} \quad (25)$$

Before scaling the derivation of the Lyapunov function $\dot{V}_1$ [29], we have

$$\begin{aligned} e_2^{\mathrm{T}}\tilde{\tau}_d &\le \frac{1}{2}e_2^{\mathrm{T}}e_2 + \frac{1}{2}\tilde{\tau}_d^{\mathrm{T}}\tilde{\tau}_d - \tilde{\tau}_d^{\mathrm{T}}\dot{\tau}_d \\ &\le \frac{1}{2}\tilde{\tau}_d^{\mathrm{T}}\tilde{\tau}_d + \frac{1}{2}\dot{\tau}_d^{\mathrm{T}}\dot{\tau}_d \\ &\le \frac{1}{2}\tilde{\tau}_d^{\mathrm{T}}\tilde{\tau}_d + \frac{1}{2}\zeta^2 - \tilde{\tau}_d^{\mathrm{T}}R(e_2)M_{jd}^{-1}(x_1)\kappa^{*\mathrm{T}}\psi(Z) \\ &\le \frac{\|R(e_2)M_{jd}^{-1}(x_1)\|^2}{2\iota} \end{aligned} \quad (26)$$

and

$$\begin{aligned} &\|\tilde{\tau}_d\|^2 + \frac{\iota}{2}\|\kappa^*\|^2\|\psi(Z)\|^2 - \tilde{\tau}_d^{\mathrm{T}}R(e_2)M_{jd}^{-1}(x_1)\nu(Z) \\ &\quad\le \frac{\left\|R(e_2)M_{jd}^{-1}(x_1)\right\|^2}{2\iota}\|\tilde{\tau}_d\|^2 + \frac{\iota}{2}\|\nu(Z)\|^2 - \sum_{i=1}^{n}\tilde{\kappa}_i^{\mathrm{T}}\sigma_i\hat{\kappa}_i \\ &\quad\le \sum_{i=1}^{n}\frac{\sigma_i}{2}\left(\left\|\kappa_i^*\right\|^2 - \|\tilde{\kappa}_i\|^2\right) \end{aligned} \quad (27)$$

where ζ is the maximum of $\|\dot{\tau}_d\|$ and ι is the arbitrary positive number that enables $R(e_2)M_{jk}^{-1}(x_1) - (1 + (((\|R(e_2)M_{jk}^{-1}(x_1)\|^2)/\iota))I > 0$. Therefore

$$\begin{aligned} \dot{V}_1 \le\ & -e_1^{\mathrm{T}}K_1e_1 - e_2^{\mathrm{T}}(K_2 - I)e_2 \\ & + e_2^{\mathrm{T}}(\hat{\kappa}^{\mathrm{T}}\psi(Z) - \kappa^{*\mathrm{T}}\psi(Z)) + \frac{1}{2}\|\bar{\nu}\|^2 \\ & - \sum_{i=1}^{n}\tilde{\kappa}_i^{\mathrm{T}}(\psi_i(Z)e_{2,i} + \sigma_i\hat{\kappa}_i) + \tilde{\tau}_d^{\mathrm{T}}\dot{\tau}_d \\ & - \tilde{\tau}_d^{\mathrm{T}}R(e_2)M_{jd}^{-1}(x_1)\nu(Z) - \tilde{\tau}_d^{\mathrm{T}}R(e_2)M_{jd}^{-1}(x_1)\tilde{\tau}_d \\ & - \tilde{\tau}_d^{\mathrm{T}}R(e_2)M_{jd}^{-1}\kappa^{*\mathrm{T}}\psi(Z) + \frac{1}{2}\zeta^2 \\ \le\ & -e_1^{\mathrm{T}}K_1e_1 - e_2^{\mathrm{T}}(K_2 - I)e_2 + \frac{1}{2}\zeta^2 \\ & - \sum_{i=1}^{n}\frac{\sigma_i}{2}\|\tilde{\kappa}_i\|^2 + \sum_{i=1}^{n}\frac{\sigma_i + \iota r^2}{2}\left\|\kappa_i^*\right\|^2 \\ & - \tilde{\tau}_d^{\mathrm{T}}\left(R(e_2)M_{jd}^{-1}(x_1) - \left[1 + \frac{\left\|R(e_2)M_{jd}^{-1}(x_1)\right\|^2}{\iota}\right)I\right] \\ & \tilde{\tau}_d + \left(\frac{1}{2} + \frac{\iota}{2}\right)\|\bar{\nu}\|^2 \\ & \le -\rho_2V_2 + C_2 \le 0 \end{aligned} \quad (28)$$

where ρ_2 and C_2, respectively, represent

$$\begin{aligned} \rho_2 = \min\Bigg(& 2\lambda_{\min}(K_1), \frac{2\lambda_{\min}(K_2 - I)}{\lambda_{\max}(M_{jd}(x_1))}, \\ & 2\lambda_{\min}\left[R(e_2)M_{jd}^{-1}(x_1) - \left(1 + \frac{\left\|R(e_2)M_{jd}^{-1}(x_1)\right\|^2}{\iota}\right)I\right], \\ & \min\left[\frac{\sigma_i}{\lambda_{\max}\left(\Gamma_i^{-1}\right)}\right]\Bigg) \end{aligned} \quad (29)$$

$$C_2 = \sum_{i=1}^{n}\frac{\sigma_i + \iota r^2}{2}\left\|\kappa_i^*\right\|^2 + \left(\frac{1}{2} + \frac{\iota}{2}\right)\|\bar{\nu}\|^2 + \frac{1}{2}\zeta^2 \quad (30)$$

$$\lambda_{\min}(K_1) > 0, \quad \lambda_{\min}(K_2 - I) > 0. \quad (31)$$

From the abovementioned analysis, we proved that error signals, e_1, e_2, $\tilde{\tau}_d$, and $\tilde{\kappa}$, are semiglobal uniform bounded.

Under the control of (19), all the condition parameters could be measured and the initiation $(x_1(0), x_2(0), \hat{\tau}_d(0), \hat{\kappa}_i(0)) \in$

Ω_0. Therefore, the error signals, e_1, e_2, $\tilde{\tau}_d$, and $\tilde{\kappa}$, were limited in Ω_{e_1}, Ω_{e_2}, $\Omega_{\tilde{\tau}_d}$, and $\Omega_{\tilde{\kappa}}$

$$\begin{aligned}\Omega_{e_1} &= \{e_1 \in \mathbf{R}^n | \|e_1\| \leq \sqrt{D}\} \\ \Omega_{e_2} &= \left\{e_2 \in \mathbf{R}^n | \|e_2\| \leq \sqrt{\frac{D}{\lambda_{\min}(M_{jd})}}\right\} \\ \Omega_{\tilde{\tau}_d} &= \{\tilde{\tau}_d \in \mathbf{R}^n | \|\tilde{\tau}_d\| \leq \sqrt{D}\} \\ \Omega_{\tilde{\kappa}} &= \left\{\tilde{\kappa} \in \mathbf{R}^{l\times n} | \|\tilde{\kappa}\| \leq \sqrt{\frac{D}{\lambda_{\min}(\Gamma^{-1})}}\right\} \end{aligned} \tag{32}$$

where $D = 2(V_2(0) + C_2/\rho_2)$, and l is the number of train nodes in neural network.

ACKNOWLEDGMENT

Youzhi Sun was well appreciated for his useful comments and suggestions for our research. His analysis of the current HDPs lets the authors fully understand the hip disarticulated amputees' experience about gait patterns and their mentality. They would also like to thank Wang Zesheng, Ban Zetao, and Zhang Wendong for their help with the experimental setup and data acquisition.

REFERENCES

[1] Y. Huang *et al.*, "Step length and velocity control of a dynamic bipedal walking robot with adaptable compliant joints," *IEEE/ASME Trans. Mechatronics*, vol. 18, no. 2, pp. 598–611, Apr. 2013.

[2] M. E. Kralovec, M. T. Houdek, K. L. Andrews, T. C. Shives, P. S. Rose, and F. H. Sim, "Prosthetic rehabilitation after hip disarticulation or hemipelvectomy," *Amer. J. Phys. Med. Rehabil.*, vol. 94, no. 12, pp. 1035–1040, Dec. 2015.

[3] H. Hara *et al.*, "Successful first gait of a child with hip-disarticulation prosthesis," *Amer. J. Phys. Med. Rehabil.*, vol. 97, no. 10, pp. e90–e92, Oct. 2018.

[4] J. Hardes *et al.*, "Endoprostheses for stump formation after hip disarticulation," *Orthopade*, vol. 48, no. 7, pp. 582–587, 2019.

[5] E. Ludwigs, M. Bellmann, T. Schmalz, and S. Blumentritt, "Biomechanical differences between two exoprosthetic hip joint systems during level walking," *Prosthetics Orthotics Int.*, vol. 34, no. 4, pp. 449–460, Dec. 2010.

[6] T. Chin, H. Oyabu, Y. Maeda, I. Takase, and K. Machida, "Energy consumption during prosthetic walking and wheelchair locomotion by elderly hip disarticulation amputees," *Amer. J. Phys. Med. Rehabil.*, vol. 88, no. 5, pp. 399–403, May 2009.

[7] Z. Dänes and A. Till, "Rehabilitation of patients after hip disarticulation," *Arch. Orthopaedic Trauma Surgery*, vol. 116, no. 8, pp. 498–499, Oct. 1997.

[8] K. Yoshikawa *et al.*, "A case of an elderly hip disarticulation amputee with rheumatoid arthritis who regained the ability to walk using a hip prosthesis," *J. Phys. Therapy Sci.*, vol. 31, no. 4, pp. 366–370, 2019.

[9] K. Carroll, "Hip disarticulation and transpelvic amputation: Prosthetic management," *Atlas of Amputations and Limb Deficiencies: Surgical, Prosthetic, and Rehabilitation Principles*, 3rd ed. Rosemont, IL, USA: American Academy of Orthopaedic Surgeons, 2004, pp. 565–573.

[10] W. Cao, C. Chen, H. Hu, K. Fang, and X. Wu, "Effect of hip assistance modes on metabolic cost of walking with a soft exoskeleton," *IEEE Trans. Autom. Sci. Eng.*, early access, Oct. 23, 2020, doi: 10.1109/TASE.2020.3027748.

[11] Z. H. Zhou, Y. Liao, C. R. Wang, and Q. N. Wang, "Preliminary evaluation of gait assistance during treadmill walking with a lightweight bionic knee exoskeleton," in *Proc. IEEE Int. Conf. Robot. Biomimetics*, 2016, pp. 1173–1178.

[12] M. Nietert, N. Englisch, P. Kreil, and G. Alba-lopez, "Loads in hip disarticulation prostheses during normal daily use," *Prosthetics Orthotics Int.*, vol. 22, no. 3, pp. 199–215, Dec. 1998.

[13] R. Davis, H. Richter, D. Simon, and A. van den Bogert, "Evolutionary optimization of ground reaction force for a prosthetic leg testing robot," in *Proc. Amer. Control Conf.*, 2014, pp. 4081–4086.

[14] Q. Wang, K. Yuan, J. Zhu, and L. Wang, "Walk the walk: A lightweight active transtibial prosthesis," *IEEE Robot. Autom. Mag.*, vol. 22, no. 4, pp. 80–89, Dec. 2015.

[15] K. Yuan, Q. Wang, and L. Wang, "Fuzzy-logic-based terrain identification with multisensor fusion for transtibial amputees," *IEEE/ASME Trans. Mechatronics*, vol. 20, no. 2, pp. 618–630, Apr. 2015.

[16] M. Li, X. Gao, Y. Wen, J. Si, and H. H. Huang, "Offline policy iteration based reinforcement learning controller for online robotic knee prosthesis parameter tuning," in *Proc. Int. Conf. Robot. Autom. (ICRA)*, 2019, pp. 2831–2837.

[17] D. Campbell and S. Robertson, "The use of snowboard boot bindings in a hip disarticulation prosthesis," *Prosthetics Orthotics Int.*, vol. 26, no. 1, pp. 76–77, Apr. 2002.

[18] E. Gailledrat *et al.*, "Does the new helix 3D hip joint improve walking of hip disarticulated amputees?" *Ann. Phys. Rehabil. Med.*, vol. 56, no. 5, pp. 411–418, Jul. 2013.

[19] D. L. Moura and A. Garruço, "Hip disarticulation—Case series analysis and literature review," *Revista Brasileira de Ortopedia*, vol. 52, no. 2, pp. 154–158, Mar. 2017.

[20] B. L. Schnall, B. S. Baum, and A. M. Andrews, "Gait characteristics of a soldier with a traumatic hip disarticulation," *Phys. Therapy*, vol. 88, no. 12, pp. 1568–1577, Dec. 2008.

[21] L. M. Nelson and N. T. Carbone, "Functional outcome measurements of a veteran with a hip disarticulation using a helix 3D hip joint: A case report," *JPO J. Prosthetics Orthotics*, vol. 23, no. 1, pp. 21–26, Jan. 2011.

[22] E. M. Ficanha, G. A. Ribeiro, L. Knop, and M. Rastgaar, "Time-varying human ankle impedance in the sagittal and frontal planes during stance phase of walking," in *Proc. IEEE Int. Conf. Robot. Autom. (ICRA)*, May 2017, pp. 6658–6664.

[23] J.-H. Kim and J.-H. Oh, "Development of an above knee prosthesis using MR damper and leg simulator," in *Proc. IEEE Int. Conf. Robot. Autom. (ICRA)*, vol. 4, 2001, pp. 3686–3691, doi: 10.1109/ROBOT.2001.933191.

[24] Y. Huang, Q. Huang, and Q. Wang, "Chaos and bifurcation control of torque-stiffness-controlled dynamic bipedal walking," *IEEE Trans. Syst., Man, Cybern. Syst.*, vol. 47, no. 7, pp. 1229–1240, Jul. 2017.

[25] W. Cao, H. Yu, W. Zhao, J. Li, and X. Wei, "Target of physiological gait: Realization of speed adaptive control for a prosthetic knee during swing flexion," *Technol. Health Care*, vol. 26, no. 1, pp. 133–144, Mar. 2018.

[26] N. Dhir, H. Dallali, E. M. Ficanha, G. A. Ribeiro, and M. Rastgaar, "Locomotion envelopes for adaptive control of powered ankle prostheses," in *Proc. IEEE Int. Conf. Robot. Autom. (ICRA)*, May 2018, pp. 1488–1495.

[27] M. M. Zhang *et al.*, "Adaptive patient-cooperative control of a compliant ankle rehabilitation robot (CARR) with enhanced training safety," *IEEE Trans. Ind. Electron.*, vol. 65, no. 2, pp. 1398–1407, Dec. 2018, doi: 10.1109/tie.2017.2733425.

[28] E. Zheng, S. Manca, T. Yan, A. Parri, N. Vitiello, and Q. Wang, "Gait phase estimation based on noncontact capacitive sensing and adaptive oscillators," *IEEE Trans. Biomed. Eng.*, vol. 64, no. 10, pp. 2419–2430, Oct. 2017.

[29] Q. Wang, J. Fu, and J. Wang, "Fully distributed containment control of high-order multi-agent systems with nonlinear dynamics," *Syst. Control Lett.*, vol. 99, pp. 33–39, Jan. 2017.